Materials Advances

PAPER

Check for updates

Exploration of charge transfer interaction, terahertz analysis, Z-scan and nonlinear optical properties of morpholinium 3,5-dinitrosalicylate (M35DNS): a spectroscopic and computational approach

M. R. Kannan,[a] Thiyagarajan Maadhu,[b] Ajinkya Punjal, [ID][c] Ruturaj Puranik,[c] Utkarsh Pandey,[c] Shriganesh S. Prabhu, [ID][c] T. C. Sabari Girisun,[d] Naini Bajaj, [ID][e] Amartya Sengupta, [ID][e] G. Vinitha [ID][f] and T. Vijayakumar [ID] *[a]

The structural, vibrational, and NLO properties of a morpholinium 3,5-dinitrosalicylate (M35DNS) crystal determined using density functional theory (DFT) to elucidate the charge transfer interaction and the influence of ionic hydrogen bonds are reported. Quantum chemical calculations are used to probe the electronic and optical properties of the given crystal. The elongation of experimentally measured $C_{13}=O_4$ and $N_{21}-H_{23}$ bonds is observed, which clearly explains the involvement of amino and carbonyl groups in the formation of strong N−H···O hydrogen bonding in the crystal. The observed simultaneous and intense activity of 8b, 14, and 18a modes in Raman and IR substantiates the charge transfer interaction in the M35DNS crystal. The low-frequency vibrational modes of the M35DNS crystal are examined using terahertz time-domain spectroscopy (THz-TDS) and terahertz-Raman spectroscopy (THz-RS) studies. Furthermore, the energy gap of 3.82 eV indicates the electron transfer from the occupied orbitals to the unoccupied orbitals in the salicylate region. Natural bond orbital (NBO) analysis predicts that the interaction between the LP (1) (C_{14}) → LP* (1) (C_{13}) shows a strong stabilization energy of 406.29 kJ mol^{-1}, substantiating the intramolecular charge transfer in the molecule. The lowest energy gap substantiates the charge transfer in the M35DNS crystal, and the chemical softness is computed to be 0.1310 eV. The dipole moment, polarizability and first order hyperpolarizability of M35DNS are estimated as 8.76 D, 2.91×10^{-23} electrostatic units (e.s.u.) and 8.9×10^{-30} e.s.u., respectively. The second harmonic generation (SHG) signal of the M35DNS crystal is measured by the powder method, which is 0.02 times the urea standard. The two-photon absorption coefficient was estimated to be 0.66×10^{-11} m W^{-1}, mainly due to the D−π···A molecular structure and the optical limiting threshold estimated to be 2.58×10^{13} W m^{-2}, enabling this material to be a potential candidate for optical limiting applications. The observed NLO properties of the M35DNS crystal can be useful for photonic, optoelectronic devices and NLO applications.

[a] Futuristic Materials Research Centre for Planetary Exploration, Department of Physics and Nanotechnology, College of Engineering and Technology, Faculty of Engineering and Technology, SRM Institute of Science and Technology, Kattankulathur, 603 203, ChengalpetTamil Nadu, India. E-mail: vijayakt1@srmist.edu.in
[b] Department of Science & Humanities-Physics, J. N. N. Institute of Engineering, Tiruvallur 601102, Tamil Nadu, India
[c] Department of Condensed Matter Physics and Materials Science, Tata Institute of Fundamental Research, Mumbai, Maharashtra 400005, India
[d] Nanophotonics Laboratory, Department of Physics, Bharathidasan University, Tiruchirapalli, Tamil Nadu 620024, India
[e] Department of Physics, Indian Institute of Technology Delhi, New Delhi 110016, India
[f] Division of Physics, School of Advanced Sciences, Vellore Institute of Technology, Chennai 600127, India
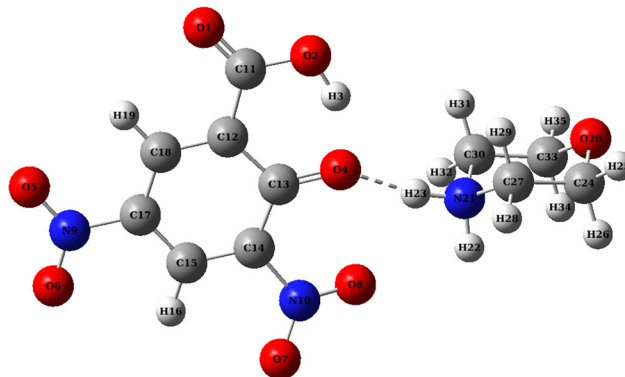
1. Introduction

Nonlinear optics (NLO) deals with the interaction of light with matter in which the response of the polarization changes nonlinearly with an electric field.[1] For the past few decades, the non-linear optical response of inorganic, organic, and semi-organic molecules has been of broad interest to researchers in many emergent fields like optical communication, electro-optics, terahertz technology, signal processing, and high-speed information.[2–7] The improvement in the molecular polarizability and hyperpolarizability of the NLO materials has received great attention in the development of optical applications.

Dipolar organic molecules, containing electron-donating and electron-accepting groups, exhibit significant second-order optical nonlinearity due to efficient intramolecular charge transfer (ICT) between these oppositely acting groups. When such organic systems are complexed with inorganic components through acid–base interactions, the resulting structures involve highly polarizable cations connected to anions *via* hydrogen-bond networks, leading to a noncentrosymmetric molecular organization that is essential for enhancing nonlinear optical (NLO) properties.[8] Morpholinium 2-chloro-4-nitrobenzoate is one such organic NLO material and it is found to be phase matchable with all nonlinear processes.[9] The vibrational spectral analysis on certain amino acid derivatives has been carried out to elucidate the correlation between the molecular structure and NLO property of ionic hydrogen-bonded NLO systems.[8]

Morpholine is a colorless, oily, volatile organic chemical molecule, a strong alkali that belongs to the secondary aliphatic amine. Furthermore, the incorporation of nitrogen into a six-member ring provides a lone pair of electrons on the nitrogen, making it a good nucleophile.[10] The morpholine with hydro halides, phenols, and phosphoric acid forms a series of molecular complexes.[11] Salicylic acid, with the chemical formula $C_7H_6O_3$, is also known as 2-hydroxybenzoic acid. It is broadly used in organic synthesis because it plays a key role in many skin-care products used to cure conditions such as keratosis pilaris, psoriasis, calluses, acne, warts, and corns.[12] Besides that, it has also been comprehensively used for the relief of inflammation, headaches, and arthritis pain for example, and furthermore, it has been used by elderly people in their recovery from heart attacks and strokes, and its many derivatives.[13] Recently, it has been used as an intermediate in the production of dyes, agrochemicals, and colorant products.[14] Also, the Raman and IR spectral investigations of various aqueous solutions of salicylic acid and its derivatives with different pH values have been reported.[15] Several single crystals derived from morpholine, such as morpholinium 4-hydroxybenzoate,[16] morpholin-4-ium P-aminobenzoate,[17] morpholinium chloroindate III,[18] morpholin-4-ium cinnamate,[19] morpholinium cinnamate,[20] morpholinium nitrate,[21] and morpholinium perchlorate[22] have been reported in the literature. In order to improve the synthesis methods, the use of computational approaches is vital to enhancing the accuracy of the characterization process and provides detailed insights into key physicochemical properties.[23]

Organic NLO materials are preferred over their inorganic counterparts due to their stronger nonlinear optical responses, faster reaction times, ease of tuning molecular properties through targeted chemical synthesis, and greater resistance to optical damage.[8] Typically, the charge transfer interaction between the cation and anion can be enhanced by the inclusion of potential donor and acceptor functional groups, resulting in large nonlinear optical responses. The efficient π-conjugation materials generally exhibit higher values of polarizability and hyperpolarizability.[24] Vibrational spectral analysis on certain amino acid derivatives has been carried out to elucidate the correlation between the molecular structure and NLO property of ionic hydrogen-bonded NLO systems, and the Terahertz
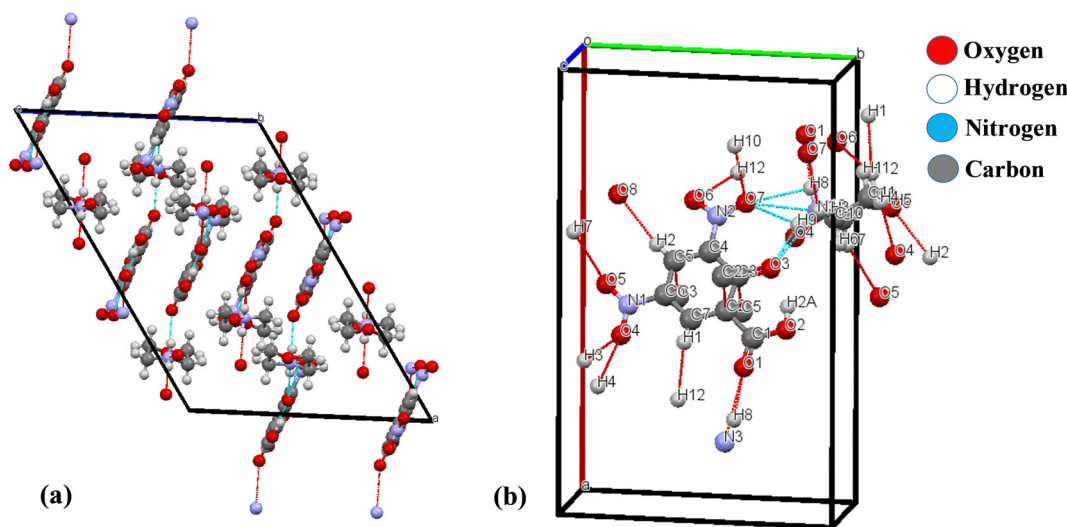

Fig. 1　Optimized structure of M35DNS.

time-domain spectroscopy (THz-TDS) method has also been used to probe the low frequency regions.

In this research work, the optical properties of a morpholinium 3,5-dinitrosalicylate (M35DNS) crystal are explored in detail for the first time. The optimized geometry parameters and vibrational spectra (FT-IR and FT-Raman) of a M35DNS crystal (Fig. 1) are examined and described using both theoretical and experimental techniques. The natural bond orbital (NBO) analysis, Frontier molecular orbital (FMO), molecular absorption studies (UV), and molecular electrostatic potential (MEP) are used to investigate the structure, electronic, and optical properties of the M35DNS crystal. The NLO properties (dipole moment, polarizability, and hyperpolarizability) are studied, and the low-frequency intermolecular interactions are examined using THz-TDS spectroscopy. A second harmonic generation (SHG) experiment is carried out to analyze the non-centrosymmetric nature of the crystal, and Z-scan studies are performed to elucidate the reverse saturable absorption (RSA), known as the two-photon absorption (TPA), and the absorption coefficient. The present work explains the structural, vibrational, and NLO properties of the M35DNS crystal through spectral investigations aided by DFT to elucidate charge transfer interactions and hydrogen bonds.

2. Materials and methods

2.1 Experimental details

The morpholinium 3,5-dinitrosalicylate (M35DNS) crystal was grown by the slow evaporation solution growth method.[25] The FTIR spectrum was obtained using a Bruker-Alpha-Platinum-ATR-IR in the region of 500–4000 cm^{-1}. The FT-Raman spectrum was recorded with an exciting wavelength of 1064 nm using an Nd-YAG laser with a resolution of 0.8 to 4 cm^{-1} and operating in the range of 50–4000 cm^{-1} using an FT-Raman spectrometer (BRUKER RFS 27 MultiRAM). An ultraviolet-visible (UV-Vis) spectrometer (SHIMADZU, UV 3600 PLUS) was used to record the ultraviolet absorption spectrum with a spectral range of the instrument of 200–900 nm.

2.2 Crystal structure

M35DNS crystallizes in the noncentrosymmetric monoclinic space group $C2/c$, and its unit cell contains one formula unit

Fig. 2 (a) Three-dimensional crystal packing diagram of the M35DNS and (b) intermolecular interactions in M35DNS.

composed of two ions of salicylate (C=O⁻ ions) and two cations of morpholinium (NH²⁺) as part of the crystallization. The cell dimensions are: a = 20.8910(5) Å, b = 10.3638 (3) Å, c = 14.6108 (2) Å, α = 90°, β = 122.553 (10)° and γ = 90°. The morpholinium cation interacts with the neighboring group of salicylate anions. The crystal packing[25] and the non-bonded interactions (indicated by red and blue dashed lines) of M35DNS are presented in Fig. 2(a) and (b).

2.3 Computational details

To examine the structural parameters, electronic distribution, and vibrational features of M35DNS the Hartree–Fock HF/6-311++G (d, p) basis set is used in the Gaussian 16 program package.[26] Furthermore, NBO analysis is performed to investigate hyperconjugation resulting from a range of intramolecular and intermolecular interactions, employing the second-order Fock matrix.[27] Subsequently, the wavenumbers were uniformly scaled down by a factor of 0.9059 to match the experimental data, and the VEDA4[28] program is employed to assign the vibrational modes using potential energy distribution (PED). To scrutinize the electronic excitations and oscillator strengths the following set (time-dependent density functional theory) TD-DFT/B3LYP/6-311++G (d, p) method was performed.[29] Finally, GaussView 6.0 software was used to display the atomic displacements and vibrational assignments.[30] Crystal Explorer program 3.1[31] was used to plot the two dimensional fingerprint map and analyze the Hirshfeld surfaces. Furthermore, the non-linear optical properties are calculated using the B3LYP/6-311++G (d, p)[32–34] basis set.

The total static dipole moment (μ), mean polarizability (α_0) and first-order hyperpolarizability (β_{tot}) are computed using eqn (1)–(3).[35]

$$\mu = \left(\mu_x^2 + \mu_y^2 + \mu_z^2\right)^{\frac{1}{2}} \quad (1)$$

$$\alpha_0 = \frac{\alpha_{xx} + \alpha_{yy} + \alpha_{zz}}{3} \quad (2)$$

$$\beta_{tot} = \left(\beta_x^2 + \beta_y^2 + \beta_z^2\right)^{\frac{1}{2}} \quad (3)$$

3. Results and discussion

3.1 Structural parameters

The optimized structural parameters (bond length, bond angle and dihedral angle) of M35DNS are calculated using the Hartree–Fock/6-311++G (d, p) basis set and the corresponding experimental values[25] are summarized in Table S1. It is found that the computed bond lengths of C–N and C–C bonds in the vicinity of the hetero atoms are slightly deviated from the observed bond length which suggests the strong influence of electronegativity of hetero atoms on the structure of the M35DNS crystal. The bond lengths of C_{12}–C_{18}, C_{17}–C_{18}, and C_{15}–C_{17} are measured as 1.373, 1.385, and 1.382 Å being calculated as 1.370, 1.392, and 1.371 Å, and are found contracted as compared to other (C_{12}–C_{13} = 1.438 and C_{13}–C_{14} = 1.431 Å) C–C bonds of the salicylate ring anion, which clearly demonstrates the influence of hetero atoms.
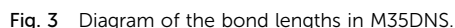
The measured bond length of the C_{13}=O_4 bond is elongated to 1.277 Å, and the N_{21}–H_{23} bond length is elongated to 1.038 Å, which clearly explains the involvement of amino and carbonyl groups in the formation of strong N–H⋯O hydrogen bonding in the crystal.

Furthermore, the observed elongation of C_{33}–O_{20} and C_{34}–O_{20} (1.408 and 1.409 Å) in the morpholinium cation and the C_{15}–H_{16} elongation in the salicylate anion clearly affirms the existence of C–H⋯O hydrogen bonding in the M35DNS crystal as shown in Fig. 3. A detailed comparison is given (Table S1) between the geometric parameters (bond lengths, bond angles, and dihedral angles) optimized using the HF/6-311++G (d, p) method and the corresponding experimental values.

3.2 Vibrational spectral analysis

A spectral study using the FT-IR and FT-Raman spectra of the M35DNS crystal is performed based on the morpholinium

Fig. 3 Diagram of the bond lengths in M35DNS.

Fig. 5 Theoretical and experimental Raman spectra of M35DNS.

cation and salicylate anion group vibrations. The morpholinium group vibration comprises amino, carbonyl, methylene, and skeletal vibrations, while the salicylate anion encompasses the phenyl ring, carboxyl, nitro, ketone and skeletal groups. The computed and experimental FT-IR and FT-Raman spectra with atomic displacements (Fig. 4 and 5) are used to identify the vibrational modes unambiguously. Furthermore, potential energy distribution (PED) calculations were performed using the VEDA4 program. The observed FTIR and FT-Raman peak positions and their computed vibrational wave numbers are presented in Table S2.

The most prominent peaks observed at 1352 cm^{-1} in IR and 1341 cm^{-1} in Raman spectra can be correlated to the combined vibrations of most of the constituents of the salicylate anion and morpholinium cation of the NLO crystal M35DNS which is predicted at 1402 cm^{-1}. The Eigenvector analysis of this mode described by the DFT studies illustrates the involvement of C=O, C=C, C–C, C–N, CH$_2$, NH$_2$ and C–O bonds corresponding to the ν(C=C/C–C) in the in-phase stretching vibrations. This vibration extends over the π-conjugated system with significant intensities at salicylate anions in the M35DNS crystal, which

involves and favors the charge transfer interaction, and provides a substantial change in dipole moment and polarizability, producing intense FT-IR and Raman activities.[25] In addition, the phenyl modes 8b, 14 and 18a along with NO$_2$ groups, are found to be strongly and simultaneously active in both IR and Raman, contributing to the linear electro-optic effect.

Salicylate anion group vibrations. The salicylate anion group consists of a phenyl ring substituted with a ketone, carboxylic acid, and nitro functional groups.

Phenyl ring. Generally, the benzene ring stretching vibrations are very prominent with a double bond in the conjugated ring.[20,36,37] With the heavy substituents, the bands tend to shift towards lower wavenumbers, and the greater the number of substituents on the ring, the broader the absorption region.[36] For asymmetric *p*-tetra substituted benzene, the doubly degenerate 8 and 19 modes appear in the wavenumber range 1650–1540 cm^{-1} and 1534–1328 cm^{-1} respectively.[37] The phenyl ring mode 8a manifests a strong band in IR at 1610 cm^{-1} and 1604 cm^{-1} in Raman and this tangential ν(C=C/C–C) stretching vibrations spread over the salicylate group.[37] Likewise, the observed very strong IR band at 1535 cm^{-1} and an intense Raman band at 1545 cm^{-1} can be correlated to the 19b mode of the salicylate ring. The intense band at 1501 cm^{-1} in IR and medium band at 1511 cm^{-1} in Raman spectra are attributed to the 19a mode along with the contribution from the deformation modes of hydroxyl, nitro, and amino groups. It is found that the 19b mode has a higher wavenumber than the 19a mode, as in other *para*-tetra substituted benzene rings. The ring modes 8a and 19b are found to be strongly and simultaneously active in both IR and Raman spectra, which is due to the charge transfer interaction between morpholinium and the salicylate group through N–H···O bonding in M35DNS.

For polysubstituted benzene derivatives, the in-plane bending C–H vibrations of 9, 15, and 18 modes appear in the region of 1000–1300 cm^{-1}. In M35DNS, the mode 9b is identified at

Fig. 4 Theoretical and experimental IR spectra of M35DNS.

1326 cm^{-1} as an intense IR band and 1316 cm^{-1} as a very strong band in the Raman spectra, being computed at 1338 cm^{-1}, while the bands observed at 1163 cm^{-1} and 1164 cm^{-1} in IR and Raman spectra, respectively, can be correlated to the 15 phenyl mode. The in-plane C–H deformation 18b mode is found at 1102 cm^{-1} as an intense IR band, which is predicted at 1149 cm^{-1}, while the 18b mode is observed at 1085 cm^{-1} and 1091 cm^{-1} in IR and Raman spectra, respectively. It is inferred that the ring C–H deformation mode 9b is found to be more active in both IR and Raman spectra simultaneously along with the chelated carbonyl, hydroxyl group, and amine and methylene groups of morpholinium cation substantiating the charge transfer interaction through N–H···O hydrogen bonding.

The aromatic C–H stretching vibrations are typically expected in the region 3100–3000 cm^{-1}.[38] In polysubstituted benzene, the ring C–H stretching mode 2 is found at 3133 cm^{-1} as a medium band in IR spectra, which is computed to be at 3094 cm^{-1} in the DFT analysis.

The out-of-plane bending vibrational modes occur in the region of 1000–675 cm^{-1}. The 12 ring mode C–H out-of-plane bending vibrations are found at 935 cm^{-1} in IR and 938 cm^{-1} in Raman spectra, while the medium IR band found at 900 cm^{-1} can be correlated to the 12 phenyl mode. The other out-of-plane vibrations, such as 5,10b, 11, 6a, 6b, and 16b have been identified and assigned unambiguously.[39]

Carboxyl vibrations. The carboxylic group exhibits O–H stretching, C=O stretching and O–H bending (out of plane) deformation vibrations. Generally, the O–H and C=O stretching vibrations appear in the ranges 3600–3500 cm^{-1} and 1700–1670 cm^{-1}, respectively[38] in IR spectra. In M35DNS, the O–H stretching vibration is found at 3417 cm^{-1} as a weak and broad IR band, and the carbonyl vibration is observed at 1742 cm^{-1} and 1695 cm^{-1} as very strong IR bands corresponding to the carboxyl group and ketone group attached to the phenyl ring. Likewise, the O–H deformation modes occur in the region 1440–1420 cm^{-1},[40] and the strong IR band at 1447 cm^{-1} can be correlated to the OH deformation mode.[36] The occurrence of all the vibrations of the carboxyl group in their respective regions explains the non-participation of the carbonyl group in the hydrogen bond formation with the morpholinium cation as confirmed by the XRD data.[25]

C–O^{-} vibrations. The C=O stretching vibrations of the ketone absorption band lies in the region of 1870–1540 cm^{-1}. The free C=O stretching vibrations occur around 1742 cm^{-1} in the IR spectra, and however, the C–O stretching vibrations influenced by different environments may be raised or lowered.[39] In M35DNS, the carbonyl stretching mode is identified at 1695 cm^{-1} as a strong broad IR band, which clearly explains the influence of hydrogen bonding on the C=O bond. The difference of free and associated C=O stretching vibrations of 47 cm^{-1} is substantiated by the increase in the C$_{13}$=O$_4$ (1.277 Å) bond compared with the C$_{11}$=O$_1$ (1.218 Å) bond by 0.059 Å as measured experimentally, which is computationally predicted to be 0.076 Å. Hence, the elongation of the C$_{13}$=O$_4$

bond and the lowering of the respective carbonyl stretching vibration reveals the formation of N–H···O ionic hydrogen bonding between the morpholinium cation and salicylate anion through amino and ketone moieties.

Nitro vibrations. The asymmetric stretching of an aromatic nitro group gives rise to a very strong band between 1560 and 1500 cm^{-1}.[20] The very intense band in IR spectra at 1447 cm^{-1} can be described as the asymmetric stretching mode of the NO$_2$ group, which is computed at 1503 cm^{-1} and the stronger electron acceptor ability of nitro groups may be influenced by the charge differences between donor and acceptor groups of the M35DNS NLO crystal. Furthermore, the presence of the strong electron-accepting nature of the nitro groups in the π-conjugated system normally enhances the NO$_2$ asymmetric stretching intensity to some extent. The symmetric stretching mode of this vibration usually appears as an intense band in both IR and Raman spectra between 1390 and 1330 cm^{-1}.[20] The symmetric stretching vibration of NO$_2$ is observed as a very intense band at 1278 cm^{-1} in IR spectra and a strong band at 1279 cm^{-1} in Raman spectra, being computed at 1338 cm^{-1}. Furthermore, the NO$_2$ scissoring mode occurs in the region between 890–835 cm^{-1}.[8] For the titled compound, the NO$_2$ scissoring mode is found at 900 cm^{-1} in IR spectra as a medium band which is computed to be 843 cm^{-1}. It is observed that the asymmetric and symmetric stretching wavenumbers are lowered by 56 cm^{-1} and the scissoring mode wavenumber is increased by 57 cm^{-1} from the corresponding computed values. The other NO$_2$ deformation vibrations are observed and assigned unambiguously with the aid of computed wavenumbers. The experimentally measured N$_9$–O$_5$, N$_9$–O$_6$, N$_{10}$–O$_7$ and N$_{10}$–O$_8$ bond lengths are 1.220 Å, 1.218 Å, 1.221 Å and 1.225 Å, respectively, while the corresponding computed bond lengths of 1.187 Å, 1.191 Å, 1.184 Å and 1.202 Å, which reveals the elongation of the N–O bond by 0.03 Å substantiating the formation of intermolecular N–H···O hydrogen bonding between the amino moiety of the morpholinium cation and nitro moiety of the salicylate anion. The intensity enhancement, lowering of stretching wavenumber, and increase in bending wavenumber of NO$_2$ vibration may be attributed to the electron-extracting effect of the acceptor groups of the push–pull NLO crystals.

Methine vibrations. Generally, the stretching vibration of the aromatic methine group is expected in the region 3100–3000 cm^{-1}, and the stretching wavenumber of the methine group slightly increases by 50 cm^{-1} when it is in the proximity of the non-carbon atom or in association with other hetero atoms attached to the phenyl ring. In M35DNS, the ring C$_{15}$–H$_{16}$ stretching mode 2 is observed at 3133 cm^{-1} as a medium IR band which is calculated at 3094 cm^{-1}. The C–H stretching wavenumber is blue-shifted by 40 cm^{-1} from the computed wavenumber, which is evident from the shortening of the C–H bond as confirmed by the XRD values. The C$_{15}$–H$_{16}$ bond length of M35DNS is calculated as 1.08 Å and the measured bond length is 0.93 Å revealing the shortening of the C$_{15}$–H$_{16}$ bond by

0.15 Å which correspondingly increases the stretching wavenumber of C_{15}–H_{16}. Hence, the blue shifting of the stretching wavenumber, variation in intensity, and shortening of the C–H bond explains the presence of C–H$\cdots$O hydrogen bonding through the oxygen atom of the morpholinium moiety and methine group of the salicylate moiety in the crystal. It is evident that the $H_{16}\cdots O_{20}$ bond length and the C_{15}–$H_{16}\cdots O_{20}$ bond angle are measured as 2.43 Å and 155°, and hence the total bond length of the C_{15}–$H_{16}\cdots O_{20}$ hydrogen bond is 3.300(3) Å[25] indicating the formation of C–H$\cdots$O intermolecular hydrogen bonding through which the charge transfer can take place from the salicylate anion to the morpholinium cation.

Morpholinium cation moieties vibrations

Amino vibrations. The stretching mode of saturated secondary amine (N–H) is expected in the region 3320–3280 cm^{-1} [20] and, however, for the hydrogen bonded amino group, the asymmetric and symmetric NH_2^+ stretching vibrations are shifted to 3300 cm^{-1} and 2780–2600 cm^{-1} respectively, due to the protonation of the secondary amino group as revealed by several amino acid derivatives.[8] The strong broad IR band identified at 3284 cm^{-1} is correlated to the asymmetric NH_2^+ stretching mode being computed at 3364 cm^{-1} and the symmetric NH_2^+ stretching mode is observed in IR spectra at 2751 cm^{-1}. The measured N_{21}–H_{23} and N_{21}–H_{22} bond lengths involved in the hydrogen bond formation with salicylate anions are found to be 0.91 Å and 0.91 Å respectively, which are elongated by 0.09 Å compared with the N–H measured bond length (0.82 Å), which is not involved in hydrogen bond formation,[25] lowering the stretching NH_2^+ wavenumbers. The experimental N_{21}–$H_{23}\cdots O_4$, N_{21}–$H_{23}\cdots O_8$, and N_{21}–$H_{22}\cdots O_1$ bond lengths and the corresponding bond angles are found to be 2.81, 2.93, 2.92 Å, and 157°, 123°,168°, respectively, as mentioned below in Table 1. The lowering of stretching wavenumbers, broadness, and elongation of N–H bond length confirm the formation of strong intermolecular N–H$\cdots$O hydrogen bonding from the ionic species of morpholinium cation to salicylate anion, which further enhances the non-centrosymmetry of the M35DNS crystal, enabling the molecule to be NLO active.[38] The deformation modes of the NH_2^+ group have been identified and assigned unambiguously, which are given in Table S2.

Methylene vibrations. The asymmetric and symmetric stretching vibrations of CH_2 groups typically occur near 2926 and 2853 cm^{-1}, respectively.[39] In M35DNS, the band

observed at 3024 cm^{-1} in IR spectra and at 2940 cm^{-1} in Raman spectra are correlated to the asymmetric and symmetric methylene vibrations. The C_{24}–H_{26} and C_{33}–H_{34} bond lengths, which participate in hydrogen bond formation, are measured as 0.97 Å while the other C–H bond lengths, which are not involved in hydrogen bond formation, are measured as 0.99 Å indicating the shortening of the C–H bond which participate in the C–H$\cdots$O hydrogen bond formation with the nitro moiety of the salicylate anion.[25] Also, the increase in the asymmetric stretching wavenumber by 46 cm^{-1} and the symmetric stretching by 88 cm^{-1} from the computed values indicate the existence of intermolecular C–H$\cdots$O hydrogen bonding between the methylene group of the morpholinium cation and nitro group of the salicylate anion.

Shifting of the stretching frequencies towards higher wavenumbers, intensity variation, and the elongation of bond length indicate the existence of C–H$\cdots$O hydrogen bonding between the morpholinium cation and salicylate anion throughout the M35DNS crystal.[41]

The increase in stretching wavenumbers, change in intensity, and the shortening of C–H bonds explain the presence of unusual C–H$\cdots$O hydrogen bonding called the "improper or blue shift hydrogen bonding" which is substantiated by XRD analysis.

Skeletal vibrations. Generally, the stretching vibrations of C–N, C–O, and C–C skeletal modes occur in the 1150–850 cm^{-1} region. The C–O stretching mode appears at 1102 cm^{-1} as a very strong band in IR spectra, and the bands observed at 935 cm^{-1} in IR spectra and at 938 cm^{-1} in Raman spectra can be correlated to the C–N stretching mode. All other skeletal modes have been identified and assigned unambiguously which are given in Table S2.

Low wavenumber vibrations of hydrogen bonds. The new vibrational modes, called "hydrogen bond modes", are formed due to the attractive interaction between the acceptor and donor moieties pertaining to elongations of X$\cdots$Y distance. These types of modes occur in the low wavenumber region between 300 and 50 cm^{-1}.[40] A strong Raman band at 93 cm^{-1} and an IR band at 98 cm^{-1} can be associated with the in-phase vibrations of all constituents of the crystal through N$\cdots$O hydrogen bonds providing the non-centrosymmetric structure that makes the M35DNS crystal be NLO active.

3.3 Natural bond orbital (NBO) analysis

The NBO analysis was performed using the NBO 3.1 program,[27] employing the Gaussian 16W package at the HF/6-311++G (d, p) level. This analysis is beneficial to enhancing our understanding of the charge transfer occurring between occupied and unoccupied orbitals.[42,43] The chemical nature and the type of interaction are studied by the Lewis and non-Lewis orbitals.[44] The NBO orbital's interaction, hybridization, and atomic charges substantiate the inter and intramolecular from the occupied and unoccupied orbitals.[44] The strong interaction of the charge transfer process is reckoned from the donor to the acceptor by the stabilization value, and mainly by the

Table 1 Hydrogen-bond geometry for the M35DNS compound [Å and °][25]

D–H$\cdots$A	D–H (Å)	H$\cdots$A (Å)	D$\cdots$A (Å)	D–H$\cdots$A[°]
N_{21}–$H_{23}\cdots O_4$	0.89	2.05	2.923 (3)	168
N_{21}–$H_{22}\cdots O_1$*	0.89	1.97	2.809 (3)	157
N_3–$H_{3B}\cdots O_7$	0.89	2.23	2.935 (2)	123
C_{15}–$H_{16}\cdots O_{20}$	0.93	2.43	3.300 (3)	155
C_{24}–$H_{25}\cdots O_6$	0.97	2.46	3.222 (3)	135

association of hyperconjugation to the delocalization of electrons.[45]

$$E^{(2)} = \frac{q_i F(i,j)^2}{\varepsilon_j - \varepsilon_i} \qquad (4)$$

In eqn (4), the symbols i and j refer to the donor and acceptor orbitals. The variables q_i, ε_i, ε_j, and $F(i,j)$ denote the orbital occupancy of the donating orbital, diagonal elements, and off-diagonal elements of the NBO Fock matrix, respectively. The term $E^{(2)}$ indicates the stabilization energy arising from the interaction between these orbitals. The Fock matrix of the second-order perturbation analysis is done for the M35DNS molecule, which is portrayed in Table S3. The highest interactions and prominent results are calculated from the lone pair to anti-bonding lone pair (LP) on the carbon atom and hetero atoms, respectively. The interaction between the LP (1) (C_{14}) → antibonding LP* (1) (C_{13}) pair orbital has a strong stabilization energy of 406.29 kJ mol^{-1} whereas the LP (3) (O_6) → $\pi^*(O_5-N_9)$ has a remarkable stabilization energy of 268.74 kJ mol^{-1} respectively, suggesting the ICT takes place within the molecule. The significant $\pi \rightarrow \pi^*$ electronic interaction is found as $\pi^*(C_{15}-C_{17}) \rightarrow \pi^*(C_{12}-C_{18})$ whose stabilization energy is 165.06 kJ mol^{-1}. Hence, these results evoke the presence of π-electron delocalization, which explains the charge transfer interaction from the Lewis orbital to non-Lewis orbital. Table S3 provides the results of the second-order perturbation theory analysis of the Fock Matrix in NBO.

3.4 Mulliken charge analysis

In the quantum mechanical calculations, Mulliken atomic charge analysis plays a pivotal role since its charges predominantly affect the dipole moment, electronic and molecular polarizability of the crystal system.[46] Mulliken atomic charges (population) have been investigated and estimated for the M35DNS crystal using the HF/6-311++G (d, p) basis set and the results are depicted in Fig. 6(b). The blue arrow indicates the highest dipole moment acts in the molecular system.

Herein, each atom with its order-of-magnitude-wise indicates the magnitude of atomic charges, in which the positive and negative charges are shown by the light green and red colors of the atoms. The large negative charges of the carbon ($C_{17} = -0.896\ e$, $C_{18} = -0.913\ e$) atoms impose less negative charge on the N_9

($-0.222\ e$) atom of the nitro group. The enormous negative charges of the three carbon ($C_{11} = -0.033\ e$, $C_{13} = -0.100\ e$, and $C_{18} = -0.913\ e$) atoms of the salicylate anion makes the neighboring carbon ($C_{12} = 1.675\ e$) atom more positively charged. Furthermore, the two nitrogen atoms ($N_9 = -0.222\ e$, $N_{10} = -0.298\ e$) of the salicylate group possess different negative charges, resulting in positive charge on ($O_5 = 0.011\ e$ and $O_7 = 0.034\ e$) and less negative charge on ($O_6 = -0.004\ e$, $O_8 = -0.021\ e$) the nitro group of the anion (salicylate), respectively. Consequently, the large electronegative oxygen atom O_4 pulls the hydrogen atom H_{23} more strongly towards itself, which leads to the bond shortening of the $N_{21}-H_{23}\cdots O_4$ bond that might distort the molecular structure of the M35DNS crystal, enabling the molecule to be NLO active through an intermolecular hydrogen bonding network.

3.5 Molecular electrostatic potential analysis (MESP)

The MESP of the optimized M35DNS structure is mapped by the GaussView 6.0 software, as shown in Fig. 7. MESP analysis represents the electron density distribution across the entire molecule through a 3D plot.[43] Different colors in the MESP represent the electrostatic potentials of different elements. The red and blue colors represent the most electronegative and electropositive potential, and the green color denotes the zero or neutral potential. Typically, there is a potential increase in the order of red < green < blue.[43] The color code of the MESP map of M35DNS is plotted between -8.649×10^{-2} and 8.649×10^2. The negative site is displayed by the deepest red color, while the positive site is shown by the deepest blue color. The negative regions are located around the oxygen (O_{20}, O_2, O_1, O_5, and O_6) and the nitrogen N_{21} atoms and these atoms behave as the electrophiles.[47] The positive regions are spread over all the hydrogen atoms (H_3, H_{13}, and H_{19}) of the carboxyl, benzene and morpholinium behave as nucleophiles.[48] Hence, it is observed that the difference in positive and negative regions reveals the reactivity of the molecule which explains the charge transfer interaction between the morpholinium cation and salicylate anion that strengthens the N–H⋯O hydrogen bonding network.

3.6 Frontier molecular orbital analysis (FMO)

The frontier molecular orbital (FMO) is very important to describe and characterize the electrical, optical, and chemical properties of any compound, and it also determines the inter
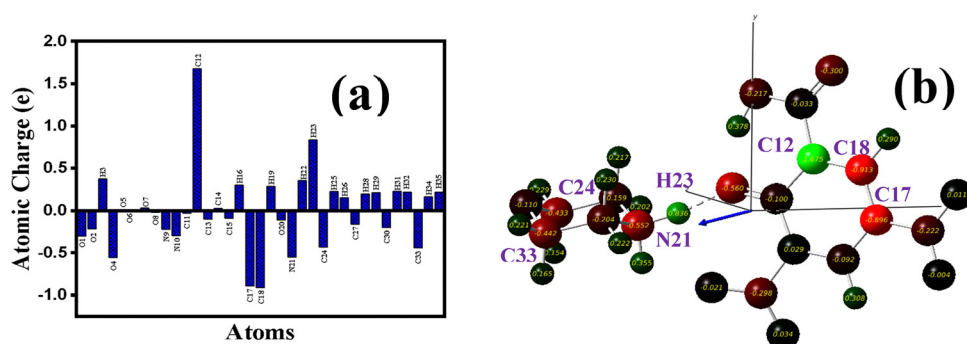

Fig. 6 Atomic charge analysis and 3D crystal structure, distinct color code, and axis along with the dipole moment vector arrow of the M35DNS crystal.
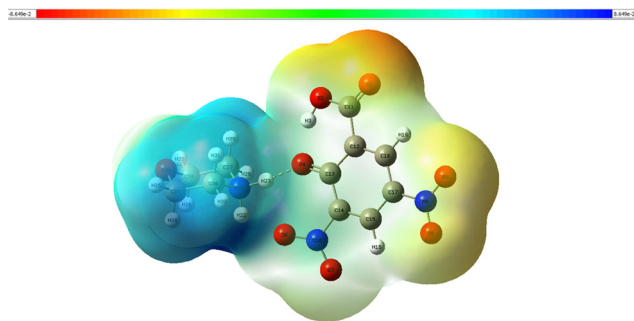
Fig. 7 Molecular electrostatic potential map of M35DNS.

and intra-molecular interactions of the other compound.[49–51] The FMO is classified into the highest occupied molecular orbital (HOMO) and lowest unoccupied molecular orbital (LUMO). The frontier molecular orbitals of the M35DNS compound are calculated using the Gaussian 16W software with the basis set of HF/6-311++G (d, p) and viewed using GaussView 6.0.16.

A three-dimensional representation of the HOMO and LUMO densities of M35DNS is displayed in Fig. 8. The green and red colors indicate the positive and negative charge over the M35DNS molecule. The HOMO electrons are delocalized over the phenyl, ketone, nitro and carboxylic groups whereas the LUMO electrons are localized over the phenyl, nitro and partially on the carboxylic group. The HOMO and LUMO energies are computed as $E_{HOMO} = -3.16$ eV and $E_{LUMO} = -6.98$ eV, respectively, and the lower energy gap (3.82 eV) clearly attributes the larger hyperpolarizability that enhances the charge transfer in the molecule.

By using the HOMO and LUMO energy of the molecule, the global reactivity descriptors such as electronegativity, chemical potential, electrophilicity, hardness and softness are quantified,[23] and are given in Table 2. The low ionization potential indicates the large molecular reactivity, whereas the higher ionization potential explains the strong stability and chemically inertness of the

Table 2 Global reactivity descriptors of M35DNS

Compound	IP	EA	X	η	μ	ω	ζ
M35DNS (eV)	6.9816	3.1671	5.074	3.8145	−5.074	3.3746	0.1310

molecule. However, the higher the electron affinity values, the larger the electron attracting capability.[45,52] The M35DNS crystal exhibits a moderately higher ionization potential (6.9816 eV) and substantially lower electron affinity of 3.1671 eV. Electronegativity describes the tendency to attract the electron or electron density towards itself, and it is found to be 5.074 eV. The potential of the electron to escape is represented by the chemical potential, and the chemical hardness upholds the stability of the material, which is determined to be 3.8145 eV and −5.074 eV, respectively, indicating that the analyzed molecule is polarizable and soft. The HOMO–LUMO energy gap for the M35DNS crystal is computed as 3.8 eV, which is in close agreement with the experimental band gap calculated from UV analysis (4.2 eV), explaining the higher kinetic stability and lower chemical reactivity. Eventually, it reveals the ionic charge transfer interaction between the morpholinium cation and salicylate anion, enabling the M35DNS molecule to be NLO active.

3.7 Optical absorption (UV) analysis

The electronic spectrum of the M35DNS crystal has been examined over the range of 200 to 900 nm. Furthermore, a theoretical electronic absorption spectrum was computed using the TD-DFT method at the B3LYP/6-311++G (d, p) level, as shown in Fig. 9. A comparison between the experimental and theoretical spectra is summarized in Table 3 that includes the wavelength (λ), oscillator strength (f) and electronic excitation energies.

The observed absorption peaks at 297, 320, and 356 nm in the UV spectrum are associated with electronic transitions
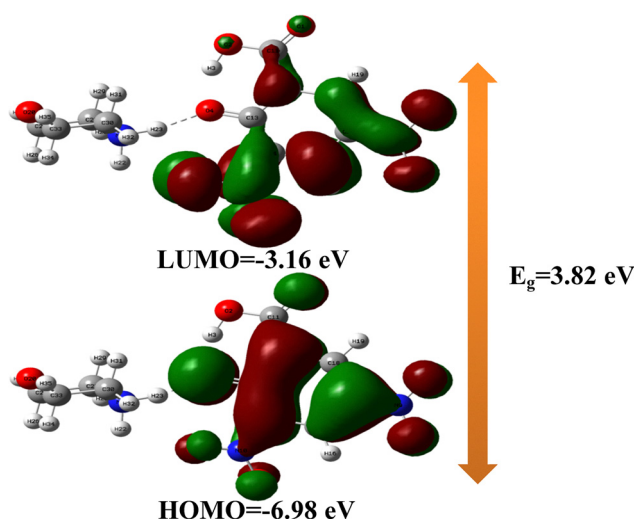

LUMO=-3.16 eV

E$_g$=3.82 eV

HOMO=-6.98 eV

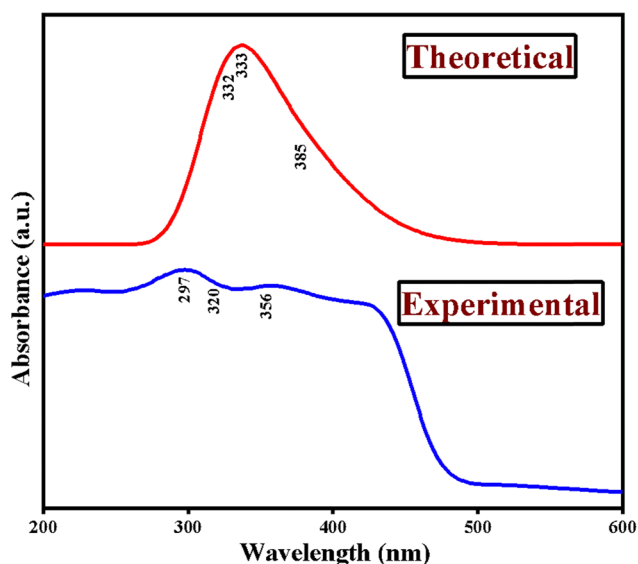Fig. 8 HOMO–LUMO plot of the M35DNS molecule.

Fig. 9 Experimental and simulated UV-visible spectra of the M35DNS crystal.

Table 3 The computed transition nature, maximum absorption wavelengths (λ_{max} in nm), and oscillator strengths (f) of M35DNS

Experimental		Theoretical				
Wave length (nm)	Band gap (eV)	Wave length (nm)	Band gap (eV)	Energy (cm^{-1})	Oscillator strength	Assignment (major and minor contributions)
356	3.48	385	3.22	25993.81	0.1235	HOMO → LUMO (97%)
320	3.87	333	3.72	30011.29	0.0413	H−6 → LUMO (24%), H−3 → LUMO (24%), H−2 → LUMO (18%), HOMO → L+1 (17%), H−1 → LUMO (5%)
297	4.17	332	3.73	30072.58	0.2802	HOMO → L+1 (75%), H−6 → LUMO (4%), H−4 → LUMO (5%), H−2 → LUMO (6%), H−1 → LUMO (4%)

resulting from changes in rotational and vibrational energy levels. It is found that the strong absorption peak occurring at 297 nm, being computed at 332 nm with an oscillator strength of 0.2802, is attributed to π–π* charge transfer transition within the M35DNS crystal.[53] Furthermore, the hypsochromic shift is attributed to the solid electron-donating characteristics of the substituents.[54,55] The energy gap of the title crystal is measured as 4.17 eV, which is computed as 3.73 eV, and the change in energy gap signifies the role of charge transfer transitions between the morpholinium cation and salicylate anion in the crystal. The calculated absorption spectra are mainly determined by HOMO → L+1 transitions at the S0 → S1 level, accounting for 75% of the contributions. Moreover, H−6 to LUMO contributes 4%, HOMO−4 → LUMO provides 5%, and H−1 → LUMO gives 4%. It is important to note that these transitions exhibit increasing oscillator strength at maximum absorption. However, it can be observed that the transition from HOMO to LUMO makes a more significant contribution to the excited state compared to the transition from HOMO−2 to LUMO, and these specific charge transfer transitions are vital in the organic crystal to exhibit their NLO activity. Since the material band gap meets the criteria for TPA when subjected to green excitation (532 nm), it satisfies the necessary conditions to be employed as an optical limiting (OL) material.

3.8 Local reactivity descriptors

Fukui functions. The local reactivity descriptors can be determined using the Fukui function, and the variations of electron densities can be observed from the variation of chemical species with respect to the change in the number of electrons of the given system. Consequently, as a result, the Fukui function reveals the tendency of the electron density has been changed at a particular point, when donating or accepting the electron. In addition, Morrel et al.,[56] recently proposed the difference between the electrophilic and nucleophilic Fukui Function, which is known as the dual descriptor and is given by the equation $\Delta f(r) = [f^+(r) - f^-(r)]$. The radical, electrophilic, and nucleophilic attacks are presented in Fig. 10(a) and the dual descriptor plot is depicted in Fig. 10(b). The atomic Fukui functions on the jth atom are performed using functions (5)–(7),

$$f_j^-(r) = q_j(N) - q_j(N - 1) \tag{5}$$

$$f_j^+(r) = q_j(N + 1) - q_j(N) \tag{6}$$

$$f_j^\bullet = \frac{1}{2}[q_j(N + 1) - q_j(N - 1)] \tag{7}$$

where $f_j^\bullet$ indicates the free radical, $f_j^-(r)$ represents the electrophilic, and $f_j^+(r)$ denotes the nucleophilic attack on the reference molecule, respectively. In the above expressed equations, the atomic charge at the jth atomic site is represented by q_j in the anionic ($N + 1$), neutral (N), and cationic ($N - 1$) forms. The nucleophilic attack is represented by $\Delta f(r) > 0$, this site is favorable and it implies the nucleophilic attack, while when $\Delta f(r) < 0$, it favors the electrophilic attack. Typically, the dual descriptor that reveals the electrophilic and nucleophilic sites of the molecule and Fig. 10(a) and (b) shows the calculated Fukui function for the active M35DNS crystal. Moreover, based on the condition of dual descriptor, the most nucleophilic site is found at C_{14}, N_{21}, and O_4 atoms (positive value). Likewise, the electrophilic site is predicted as C_{13}, H_{23}, and O_7 atoms (negative value). The M35DNS crystal has more nucleophilic (C_{14}) attack than electrophilic (C_{13}) and radial attacks (C_{17}). The analyzed results of the Fukui function analysis are in good agreement with the MESP results.

In M35DNS, the carbon (C_{14}), oxygen (O_4), and nitrogen (N_{21}) atoms exhibit larger electronegativity than the hydrogen atoms making the hydrogen atoms highly electron deficient and more prone to nucleophilic attack. Moreover, the carbon (C_{13}), hydrogen (H_{23}) and oxygen (O_7) atoms possess less electronegativity due to the presence of hetero atoms in the molecule, and are more prone to electrophilic attack. Hence, the carbon atom (C_{14}) is the most favorable site for the nucleophilic attack, and the C_{13} atom behaves like a more favorable site for the electrophilic attack.

3.9 Hirshfeld surface analysis (HS)

The HS analysis plays an important role in identifying the details of intermolecular interactions of the molecule and its proximity to neighbors. The HS (Fig. S1) and 2D fingerprint plots (Fig. S2) are generated using Crystal Explorer 3.1 software.[31] The HS analysis has been mapped over d_{norm}, shape index, d_e, d_i, and 2D fingerprint plots. Furthermore, the d_{norm} has been shown with the intermolecular contacts using the color scale. Here, red indicates distances shorter than van der Waals (vdW) separations, white indicates distances equal to vdW separations, and blue indicates distances longer than vdW separations. The pie chart (Fig. S3) illustrates the percentage contribution with the distinct regions to the whole HS area. From the pie chart, the high contact area observed for O···H is 32.3%. Besides, the maximum contributions of H···O, H···C interactions resulting from hydrogen bonds on the HS surface
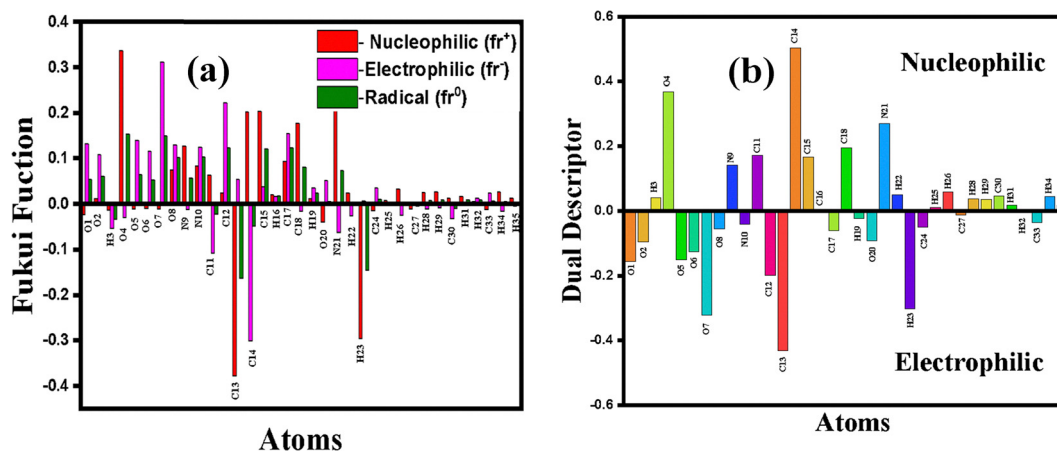
Fig. 10 (a) and (b) Local reactivity descriptor of M35DNS.

of the M35DNS crystal are 28.7 and 15.6%, respectively. It is inferred from the pie chart that the observed high contact area for O···H is 32.3%. Besides, the maximum contributions of H···O, H···C interactions resulting from hydrogen bonds in the HS surface of the M35DNS crystal are 28.7 and 15.6 %, respectively. Further, the moderate and lesser contributions from H···N, N···C, C···C, N···O, etc. interactions are due to the distance between the interacting atoms having less dispersion force or significantly greater. Moreover, the shape index and curvedness of the molecule indicate the various interactions occur within the M35DNS crystal.

3.10 NLO properties of M35DNS

When light interacts with NLO materials, it enhances their NLO activity and produces new fields with different amplitudes, frequencies or other propagation characteristics compared with the incident fields.[57] Theoretical investigations are essential in developing novel NLO compounds by uncovering their structure–property relationships. Organic materials that can manipulate photonic signals efficiently are of importance in technologies such as optical computing, optical data storage, and laser technology.[25,58] The static dipole moment, polarizability, and hyperpolarizability of the M35DNS crystal determined using the DFT/B3LYP/6-311++G (d, p) method are reported in Table 4.

The most significant transitions influencing the hyperpolarizability contribution in the M35DNS crystal predominantly occur along the x-axis (β_{xxx}), while the primary contribution to polarizability is also along the x-axis (α_{xx}). The average polarizability, dipole moment and static first-order hyperpolarizability are found to be 2.93×10^{-23} e.s.u., 8.762 D, and 8.9×10^{-30} e.s.u., respectively.

3.11 Second harmonic generation analysis (SHG)

An experiment using a small amount of crystalline powder was used to determine the SHG. In the following experimental setup, an amplified laser with a repetition rate of 1 kHz and a wavelength of 800 nm was employed and shown in Fig. 11. The laser beam was concentrated onto the sample through a

Table 4 Calculated dipole moments (D), polarizability, and first order hyperpolarizability components (a.u.) of M35DNS

Parameters	B3LYP/6-311++G (d, p)	Parameters	B3LYP/6-311++G (d, p)
μ_x	−5.55	β_{xxx}	1143.714
μ_y	−1.30	β_{xxy}	−591.675
μ_z	0.46	β_{xyy}	−418.817
μ (D)	8.762	β_{yyy}	−155.308
α_{xx}	268.33	β_{xxz}	130.728
α_{xy}	1.33	β_{xyz}	−86.716
α_{yy}	212.400	β_{yyz}	−57.866
α_{xz}	10.650	β_{xzz}	−23.113
α_{yz}	3.747	β_{yzz}	−18.458
α_{zz}	120.642	β_{zzz}	−34.339
α_{tot} (e.s.u.)	2.97×10^{-23}	β_{tot} (e.s.u.)	8.9×10^{-30}

40 cm lens. The size of the second harmonic generation (SHG) spot was determined using the Newport beam profiler, and the width at 80% intensity was measured to be 240 μm. The lens was utilized to collect the reflected light, which was focused onto the fiber. Subsequently, the second harmonic generation (SHG) signal was quantified by an Ocean Optics FX spectrometer, with the measurement conducted across various input fluence levels on the sample.[59] Eventually, the second harmonic radiation at 400 nm was obtained. Furthermore, the resulting output was filtered using a second harmonic separator to eliminate the fundamental input radiation. Moreover, a femtosecond (fs) laser with a wavelength of 800 nm was used to detect the NLO properties. The SHG was estimated to be 0.02 times that of urea and the results in Fig. 12(a) and (b) indicate that the M35DNS crystal is reasonably phase matchable. The identified peak is centered at 400 nm, precisely at half the wavelength of the incident laser. This phenomenon, known as second harmonic generation (SHG), involves the doubling of the frequency. This suggests that M35DNS possesses a noncentrosymmetric structure, as it lacks inversion symmetry. This absence of inversion symmetry is responsible for the obvious second-order nonlinearity. The variations in SHG intensities for both urea and M35DNS were recorded in relation to the incident power, as depicted in Fig. 12(a)–(c). The SHG peak undergoes a substantial increase in intensity as the input power
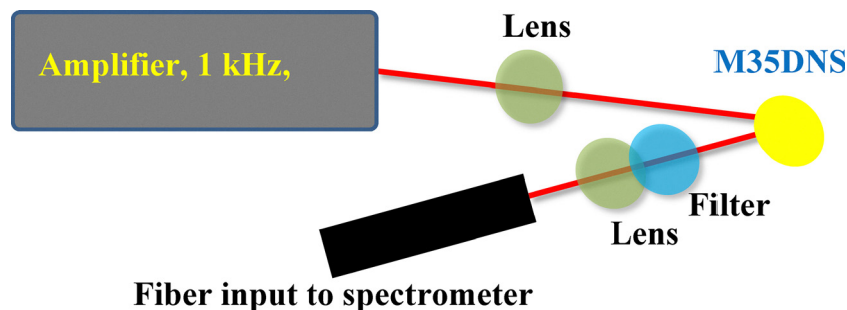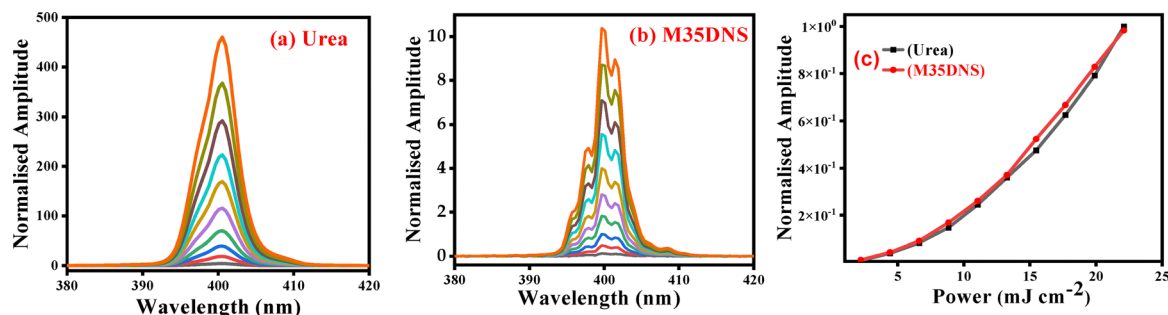
Fig. 11 Second harmonic generation setup.

Fig. 12 Second harmonic generation comparison of (a) urea, (b) M35DNS, and (c) M35DNS and urea.

is raised from 2 to 22 mJ cm^{-2} hence, as a result, the second harmonic response of M35DNS is detected at 400 nm as a strong and sharp peak confirms the SHG behavior and the nature of the sample was compared with urea allowing M35DNS material to substantiate and it can be exploited for NLO applications.

3.12 Terahertz time domain (THz-TDS) and Terahertz Raman spectroscopy (THz-RS) analysis

THz-Raman measurements were performed on the M35DNS sample using a commercial fiber-coupled ultra-high through-put Raman spectroscopy system – alpha 300R – confocal micro-Raman imaging from WiTec in a backscattering geometry with a 400 mm focal length lens-based spectrometer. THz-Raman data were obtained using a 633 nm laser, focused on the sample using a 20× objective with a laser power of $\sim$20 mW to avoid local heating in the -100 to 200 cm^{-1} spectral range and the data were collected using a CCD detector. The laser cut-off was at 5 cm^{-1} using customized Bragg filters.

M35DNS sample pellets were prepared with PTFE (polytetra-fluoroethylene) (particle size $\sim$20 µm with a density of 2.15 g cm^{-3}) in (50:100) mg mg ratio for THz-TDS measurements in the 0.2–5 THz spectral range. The pellets were prepared by placing the powder in a 13 mm diameter stainless steel (SS) die set and compressed by applying a 3-ton load for 2 mins.

THz-TDS measurements were performed on the prepared pellets using a Toptica® Teraflash PRO system. A femtosecond laser pulse with a central wavelength of 1560 nm and 80 mW power is used to generate THz at the emitter photoconductive antenna (PCA), and the same pulse is used for gated detection

of the THz pulse. The average power of the THz pulse generated in this system is $\sim$50 µW, and the repetition rate is 80 MHz. The typical bandwidth of the system goes up to 5 THz with a peak dynamic range of more than 90 dB (at 0.9 THz). We placed the entire setup inside a plexiglass box purged with nitrogen gas to avoid THz absorption by water vapor. The average humidity inside the box was measured to be $\sim$6.2 $\pm$ 1% and the average temperature to be $\sim$24.2 $\pm$ 1 °C. The THz pulse was sampled for a scan range of 100 ps by the probe pulse and from each point the THz response was recorded by averaging 2000 traces. Firstly, we measured transmission spectra through PTFE (which is the reference signal, $E_{\text{ref}}(t)$) and then with PTFE + pre-heated sample pellets through the same aperture and geometry (which is the sample signal, $E_{\text{sam}}(t)$). The THz temporal waveforms were Fast Fourier Transformed (FFT) to obtain frequency-dependent amplitude and phase. Since the sample was highly diluted, real (n) and imaginary (k) parts of the complex refractive index were obtained using eqn (8) and (9):

$$n = 1 - \frac{(\phi_s - \phi_{\text{ref}})c}{2\pi fd} \quad (8)$$

$$k = \frac{c}{2\pi fd}\log\left(\frac{4n}{(1+n)^2 \times T\left(\frac{E_s}{E_{\text{ref}}}\right)}\right) \quad (9)$$

where ϕ is the phase difference (subscript s stands for the sample and ref stands for the reference), c is the velocity of light in vacuum, f is the frequency in THz, d is the thickness of the pellet, and T is the transmission through the sample.

Paper

The variation of amplitude and $2nk$ of M35DNS is shown in Fig. 13b. The real (ε') and imaginary (ε'') parts of the dielectric function (ε) were calculated as $\varepsilon' = (n^2 - k^2)$ and $\varepsilon'' = (2nk)$.

The THz-TDS results illustrate that some weak absorption peaks are observed in the lower frequency region and a sharp peak at around 30 cm^{-1}. On the other hand, the THz-RS shows three sharp peaks at 31, 40, and 50 cm^{-1}. These low-frequency modes of THz-TDS and THz-RS vibrations arise mainly by out-of-plane bending and torsion modes of the cation and anion. The presence of 30, 47, and 58 cm^{-1} is common in both THz-TDS and THz-RS, which signifies the intramolecular charge transfer and is shown in Fig. 13, due to the non-centrosymmetric[60] nature of M35DNS, which exhibits a few more peaks in it. To the best of our knowledge, no DFT or experimental studies have reported these peaks in this range. The corresponding assignments are given in Table S2.

3.13 Z-scan analysis

Generally, organic compounds are good candidates for non-linear optical absorption applications as they exhibit high nonlinear absorption coefficients. The nonlinear optical absorption can be predicted *via* Z-scan analysis. In this analysis the transmittance was measured by varying the sample position through the focus without the aperture at the detector.[61] The Q-switched

Nd:YAG laser with 532 nm wavelength, 9 ns pulse rate, 10 Hz frequency and 100 μJ pulse energy was used for excitation. The open aperture plot of M35DNS is illustrated in Fig. 14. This clearly indicates, when the sample is placed far away, the transmittance remains constant and when it is moved towards the focus, it decreases abruptly. Thus, it shows the valley like open aperture Z-scan pattern which obviously confirms that the M35DNS exhibits the reverse saturable absorption (RSA) behavior. This clearly shows that the excited state cross-section is much higher than the ground state cross-section of M35DNS resulting in multi-photon absorption. Here, the experimental data fit well with the theoretical normalized transmittance extracted from the TPA equation. Eqn 10 was used to calculate the normalized transmittance for n-photon absorption.

$$T_{nPA} = \frac{1}{\left[1 + (n-1)\beta_n L \left(\dfrac{I_0}{1 + \left(\dfrac{z}{z_0}\right)^2}\right)^{n-1}\right]^{\frac{1}{n-1}}} \tag{10}$$

where β_n signifies the absorption coefficient and here $n = 2$, z is the sample position, and $z = \dfrac{\pi\omega_0^2}{\lambda}$ is the Rayleigh range. Thus, the RSA
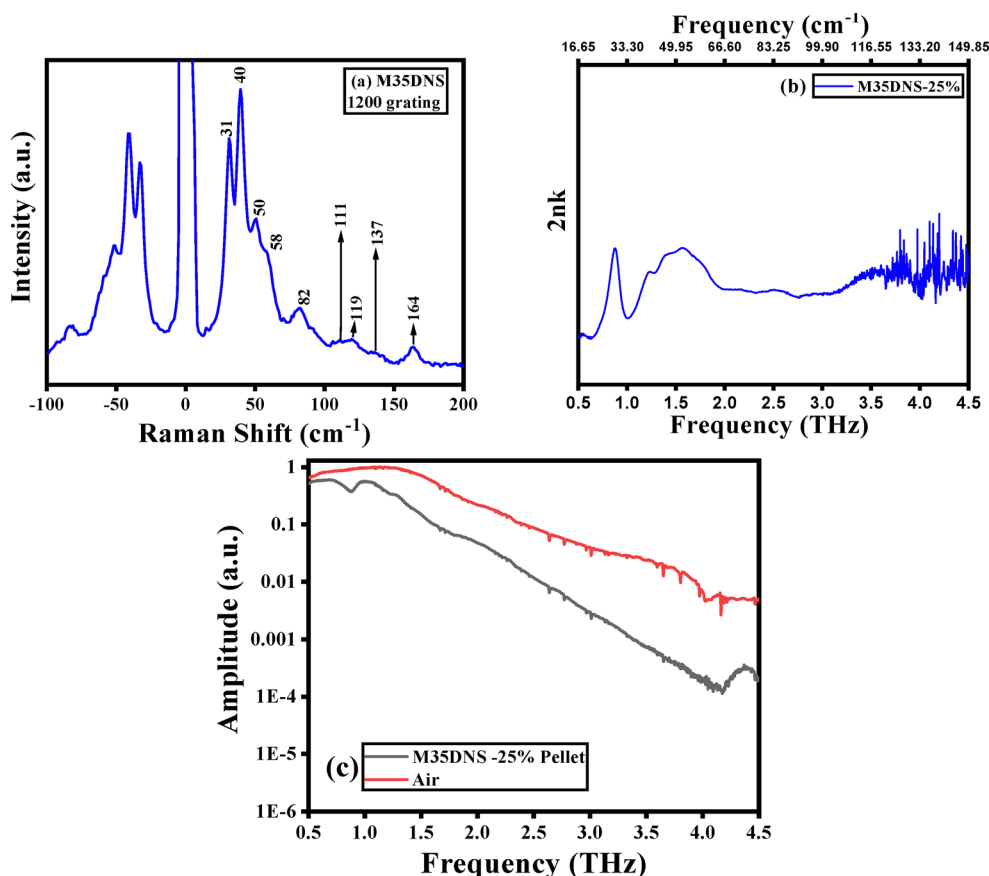

Fig. 13 (a) THz-Raman spectrum of M35DNS measured in the −100 to 200 cm^{-1} spectral range using 1200 grooves per mm grating with an exposure time of 5 seconds and 20 accumulations. (b) Variation of $2nk$ with frequency ranging from 0.5 to 4.5 THz. (c) Amplitude variation of air and M35DNS in the 0.5–4.5 THz spectral range obtained using time domain-THz spectroscopy.
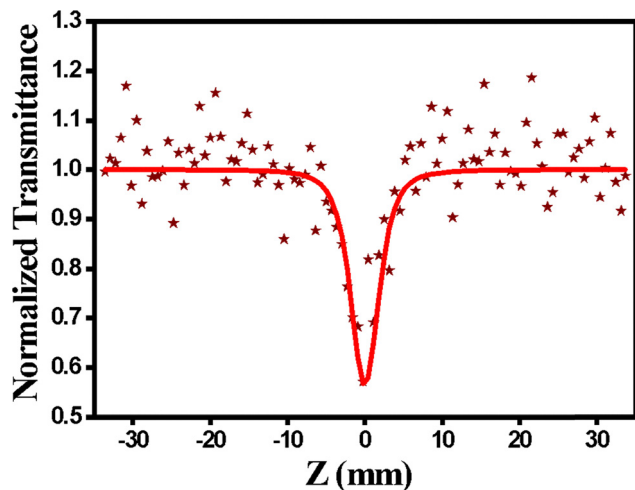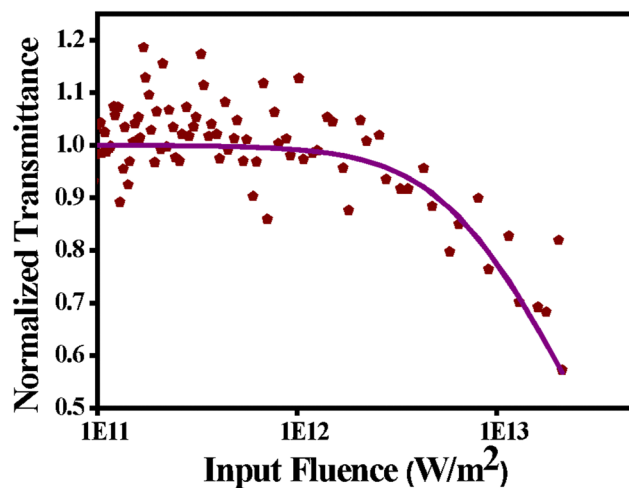
Fig. 14   Open aperture pattern of M35DNS.

Fig. 15   Optical limiting curves for M35DNS.

nature of M35DNS can be ascribed due to the TPA process. In general, TPA can occur only when the excitation energy is least half the band gap of the material. From the UV-Vis absorbance spectrum, it can be observed that the M35DNS exhibits strong absorbance in UV region at 297 nm with a corresponding energy state of 4.17 eV and this satisfies the condition for the TPA process. Consequently, under green laser excitation, the M35DNS absorbs two photons to transfer the electron from the ground state to the higher excited state. It is to be mentioned that, as the material exhibits negligible absorption in the green region, TPA occurs through simultaneous absorption of two photons, generally called genuine TPA. The estimated TPA coefficient of M35DNS is 0.66×10^{-10} m W^{-1}. Hence, M35DNS can be utilized in the field of the laser with the aid of energy absorbing NLO device fabrications.[61]

3.14   Optical limiting properties

The optical limiting (OL) properties of the grown crystal were investigated using an open aperture Z-scan method. The OL threshold is defined as where the incident laser fluence at the sample falls to half of its linear transmittance. Here, the threshold plays an important role to recognize the quality of an optical limiter.[62] Fig. 15 shows the OL behavior of the M35DNS crystal for nanosecond pulsed (100 μJ, 532 nm) laser irradiance. The fluence as a function of sample position can be estimated using eqn (11),

$$F(z) = \frac{\left[4\sqrt{\ln(2)} \frac{P_{in}}{\pi^{\frac{3}{2}}} \right]}{\omega(z)^2} \text{W cm}^{-2} \qquad (11)$$

where $F(z)$ is the input fluence, P_{in} is the excitation laser power, and ω is the laser beam radius at the focus.

When the materials show the constant transmittance at the lower input fluences and conversely the transmittance is decreased at the high input fluences this kind of process is known as OL.[63] The OL mainly depends on the nonlinear absorption of the material.[62] Fig. 15 plots normalized transmittance as a function of input influence and it shows that the

Table 5   Non-linear optical coefficients of M35DNS

Nonlinear 2PA coefficient, β ($\times 10^{-11}$ m W^{-1})	Onset optical limiting threshold ($\times 10^{11}$ W m^{-2})	Optical limiting threshold ($\times 10^{13}$ W m^{-2})
0.66	70	2.58

transmittance decreases while increasing the input fluence. The observed OL characteristics can be ascribed due to the TPA process. The OL threshold was estimated to be 2.58×10^{12} W m^{-2}. The obtained, nonlinear optical absorption coefficient, saturation intensity and OL threshold of the crystal are listed in Table 5. Thus, it can be concluded that the crystal exhibits good OL properties and furthermore, it can be used for laser safety applications.

4. Conclusion

The non-linear optical (NLO) characteristics of the M35DNS crystal have been explored through comprehensive studies such as vibrational spectrometry (Raman and IR), measurements of second harmonic generation (SHG), optical limiting assessments employing the Z-scan technique, and a detailed examination of low-frequency vibration using terahertz spectroscopy. The measured bond length of the $C_{13}=O_4$ bond was elongated to 1.277 Å, and the N_{21}–H_{23} bond length was elongated to 1.038 Å, which clearly explains the involvement of amino and carbonyl groups in the formation of strong N–H···O hydrogen bonding in the crystal. The ring modes 8b, 14, and 18a are found to be strongly and simultaneously active in both IR and Raman spectra, which is due to the charge transfer interaction between morpholinium and the salicylate group through N–H···O bonding in the M35DNS crystal. The negative regions are located around the oxygen (O_{20}, O_2, O_1, O_5, and O_6) and the nitrogen N_{21} and these atoms are related to the electrophilicity. The positive regions are placed around all the hydrogen atoms of the H_3, H_{13}, and H_{19} in the carboxyl

and benzene groups. The interaction between the LP (1) (C_{14}) → antibonding LP* (1) (C_{13}) pair orbital has a strong stabilization energy of 406.29 kJ mol^{-1}, whereas the LP (3) (O_6) → $\pi^*(O_5–N_9)$ have a remarkable stabilization energy of 268.74 kJ mol^{-1} respectively, which signifies the ICT within the molecule. Using an FMO, the computed HOMO and LUMO energy gap value was 3.82 eV. Furthermore, the calculated chemical hardness is 3.8145 eV, paired with a high negative chemical potential of −5.074 eV, which describes a soft and polarizable molecule. Moreover, the M35DNS crystal has more nucleophilic (C_{14}) attack than electrophilic (C_{13}) and radial attacks (C_{17}). The average polarizability, dipole moment, and static first-order hyperpolarizability are 2.97×10^{-23} e.s.u., 8.762 D, and 8.9×10^{-30} e.s.u., respectively. Additionally, the second harmonic response of the M35DNS crystal detected at 400 nm as a strong and sharp peak confirms the SHG nature of the sample compared with urea. Furthermore, the THz-TDS and THz-RS studies show the intramolecular charge transfer in the low-frequency region. The TPA coefficient was estimated to be 0.66×10^{-11} m W^{-1}, mainly due to the D–$\pi\cdots$A molecular structure and the OL threshold estimated to be 2.58×10^{13} W m^{-2}, enabling this material to be a potential candidate for OL applications.

Conflicts of interest

There are no conflicts to declare.

Data availability

The authors declare that the data will be made available upon request.

Supplementary information is available. See DOI: https://doi.org/10.1039/d5ma00516g.

Acknowledgements

References

1 E. Polo-Cuadrado, E. Osorio, K. Acosta-Quiroga, P. A. Camargo-Ayala, I. Brito, J. Rodriguez, J. B. Alderete, O. Forero-Doria, E. F. Blanco-Acuña and M. Gutiérrez, RSC Adv., 2024, **14**, 10199–10208.

2 S. Balaprabhakaran, J. Chandrasekaran, B. Babu, R. Thirumurugan and K. Anitha, Spectrochim. Acta, Part A, 2015, **136**, 700–706.

3 K. Rao, A. Chaudhary, M. Venkatesh, K. Thirupugalmani and S. Brahadeeswaran, Curr. Appl. Phys., 2016, **16**, 777–783.

4 M. Shalaby, C. Vicario, K. Thirupugalmani, S. Brahadeeswaran and C. P. Hauri, Opt. Lett., 2016, **41**, 1777–1780.

5 G. Shanmugam, M. Belsley, D. Isakov, E. de Matos Gomes, K. Nehru and S. Brahadeeswaran, Spectrochim. Acta, Part A, 2013, **114**, 284–292.

6 K. Thirupugalmani, S. Karthick, G. Shanmugam, V. Kannan, B. Sridhar, K. Nehru and S. Brahadeeswaran, Opt. Mater., 2015, **49**, 158–170.

7 X. Zhang, M. Li, Z. Shi and Z. Cui, Mater. Lett., 2011, **65**, 1404–1406.

8 T. Vijayakumar, I. Hubert Joe, C. Reghunadhan Nair and V. Jayakumar, J. Raman Spectrosc., 2009, **40**, 18–30.

9 S. Karthick, K. Thirupugalmani, G. Shanmugam, V. Kannan and S. Brahadeeswaran, J. Mol. Struct., 2018, **1156**, 264–272.

10 A. Arunkumar and P. Ramasamy, J. Cryst. Growth, 2014, **388**, 124–131.

11 R. Renugadevi and R. Kesavasamy, Adv. Condens. Matter Phys., 2014, **2014**, 834760.

12 K. D. Rainsford, Aspirin and the Salicylates, Elsevier, 2013.

13 S. Zaugg, X. Zhang, J. Sweedler and W. Thormann, J. Chromatogr. B: Biomed. Sci. Appl., 2001, **752**, 17–31.

14 A. S. El-Shahawy, Spectrochim. Acta, Part A, 1988, **44**, 903–907.

15 B. Humbert, M. Alnot and F. Quilès, Spectrochim. Acta, Part A, 1998, **54**, 465–476.

16 H. Ratajczak, J. Baran, J. Barycki, S. Debrus, M. May, A. Pietraszko, H. Ratajczak, A. Tramer and J. Venturini, J. Mol. Struct., 2000, **555**, 149–158.

17 G. S. Bahra, P. A. Chaloner, L. M. Dutta, W. Healy and P. B. Hitchcock, J. Cryst. Growth, 2001, **225**, 474–478.

18 G. Shanmugam, K. R. Kumar, B. Sridhar and S. Brahadeeswaran, Mater. Res. Bull., 2012, **47**, 2315–2323.

19 M. Owczarek, P. Szklarz, M. Moskwa and R. Jakubas, CrystEngComm, 2018, **20**, 703–709.

20 B. C. Smith, Infrared spectral interpretation: a systematic approach, CRC press, 2018.

21 R. Bhuvaneswari, B. Subash and K. S. Murugesan, 2019.

22 S. Swaminathan, G. Murthy and L. Lessinger, Acta Crystallogr., Sect. B: Struct. Sci., Cryst. Eng. Mater., 1976, **32**, 3140–3142.

23 C. Shiny, A. A. Kumar, C. D. Vincy, X. D. Dexlin, J. D. Tarika and T. J. Beaula, J. Mol. Struct., 2023, **1291**, 135890.

24 R. Bhuvaneswari, M. D. Bharathi, G. Anbalagan, G. Chakkaravarthi and K. S. Murugesan, J. Mol. Struct., 2018, **1173**, 188–195.

25 T. Maadhu and G. Vinitha, *J. Mater. Sci.: Mater. Electron.*, 2022, **33**, 20911–20928.

26 M. Frisch, *Gaussian 16, Revision B.01*, 2016, **1**.

27 E. Glendening, A. Reed, J. Carpenter and F. Weinhold, *NBO Ver 3.1*, Gaussian Inc., Pittsburgh, PA, 2003.

28 M. H. Jamróz, *Spectrochim. Acta, Part A*, 2013, **114**, 220–230.

29 R. Bauernschmitt and R. Ahlrichs, *Chem. Phys. Lett.*, 1996, **256**, 454–464.

30 R. Dennington, T. A. Keith and J. M. Millam, *GaussView 6.0. 16.*, Semichem Inc., Shawnee Mission KS, 2016.

31 M. A. Spackman and D. Jayatilaka, *CrystEngComm*, 2009, **11**, 19–32.

32 R. G. Parr and W. Yang, *Annu. Rev. Phys. Chem.*, 1995, **46**, 701–728.

33 R. G. Parr, 1989.

34 A. D. Becke, *J. Chem. Phys.*, 1993, **98**, 5648–5652.

35 F. Hussain, R. Hussain, M. Adnan, S. Muhammad, Z. Irshad, M. U. Khan, J. Yaqoob and K. Ayub, *RSC Adv.*, 2022, **12**, 25143–25153.

36 H. T. Varghese, C. Y. Panicker, D. Philip, J. Chowdhury and M. Ghosh, *J. Raman Spectrosc.*, 2007, **38**, 323–331.

37 G. Varsányi, *Vibrational spectra of benzene derivatives*, Elsevier, 2012.

38 D. Lin-Vien, N. B. Colthup, W. G. Fateley and J. G. Grasselli, *The handbook of infrared and Raman characteristic frequencies of organic molecules*, Elsevier, 1991.

39 R. M. Silverstein and G. C. Bassler, *J. Chem. Educ.*, 1962, **39**, 546.

40 T. Vijayakumar, I. Hubert Joe, C. Reghunadhan Nair, M. Jazbinsek and V. Jayakumar, *J. Raman Spectrosc.*, 2009, **40**, 52–63.

41 A. Venkateswaran, M. Karnan and R. Muthukumar, *J. Chem. Inf. Model.*, 2009, **9**, 835–868.

42 N. Arif, Z. Shafiq, S. Noureen, M. Khalid, A. Ashraf, M. Yaqub, S. Irshad, M. U. Khan, M. N. Arshad and A. A. C. Braga, *RSC Adv.*, 2023, **13**, 464–477.

43 O. Concepcion, A. Ali, M. Khalid, A. F. de la Torre, M. U. Khan, A. R. Raza, G. M. Kamal, M. F. U. Rehman, M. M. Alam and M. Imran, *ACS Omega*, 2021, **6**, 26016–26025.

44 A. E. Reed, L. A. Curtiss and F. J. C. R. Weinhold, *Chem. Rev.*, 1988, **88**, 899–926.

45 M. U. Khan, S. Hussain, M. A. Asghar, K. S. Munawar, R. A. Khera, M. Imran, M. M. Ibrahim, M. M. Hessien and G. A. Mersal, *ACS Omega*, 2022, **7**, 18027–18040.

46 M. F. Zaini, W. M. Khairul, S. Arshad, M. Abdullah, D. A. Zainuri, R. Rahamathullah, M. I. Rosli, M. S. Abd Aziz and I. A. Razak, *Opt. Mater.*, 2020, **107**, 110087.

47 M. Karabacak and E. Yilan, *Spectrochim. Acta, Part A*, 2012, **87**, 273–285.

48 M. Karabacak, M. Kurt, M. Cinar, S. Ayyappan, S. Sudha and N. Sundaraganesan, *Spectrochim. Acta, Part A*, 2012, **92**, 365–376.

49 M. Suriya, B. M. Boaz and K. S. Murugesan, *Appl. Phys. A: Mater. Sci. Process.*, 2019, **125**, 1–17.

50 A. Mahmood, S. U. D. Khan, U. A. Rana, M. R. S. A. Janjua, M. H. Tahir, M. F. Nazar and Y. Song, *J. Phys. Org. Chem.*, 2015, **28**, 418–422.

51 R. Hussain, M. Adnan, K. Atiq, M. U. Khan, Z. H. Farooqi, J. Iqbal and R. Begum, *Sol. Energy*, 2023, **253**, 187–198.

52 R. G. Pearson, *J. Am. Chem. Soc.*, 1985, **107**, 6801–6806.

53 S. Suresh, S. Gunasekaran and S. Srinivasan, *Spectrochim. Acta, Part A*, 2014, **132**, 130–141.

54 T. Yoshikawa, M. Kawamoto, T. Fujihara, K. Tada, T. Sassa and Y. Kawabe, *J. Opt. Soc. Am. B*, 2015, **32**, 622–627.

55 K. Kinashi, T. Fukami, Y. Yabuhara, S. Motoishi, W. Sakai, M. Kawamoto, T. Sassa and N. Tsutsumi, *NPG Asia Mater.*, 2016, **8**, e311.

56 C. Morell, A. Grand and A. Toro-Labbé, *J. Phys. Chem. A*, 2005, **109**, 205–212.

57 Y. R. Sharma, *Elementary organic spectroscopy*, S. Chand Publishing, 2007.

58 A. Ali, M. Khalid, K. P. Marrugo, G. M. Kamal, M. Saleem, M. U. Khan, O. Concepción and A. F. de la Torre, *J. Mol. Struct.*, 2020, **1207**, 127838.

59 M. Kannan, A. Punjal, R. Puranik, U. Pandey, S. Prabhu, T. S. Girisun and T. Vijayakumar, *Spectrochim. Acta, Part A*, 2023, **303**, 123175.

60 K. Singh, D. Garg, A. Bandyopadhyay and A. Sengupta, *Spectrochim. Acta, Part A*, 2022, **271**, 120923.

61 T. D. Willington, S. Joema, S. Sindhusha and T. S. Girisun, *J. Mater. Sci.: Mater. Electron.*, 2021, **32**, 25444–25461.

62 P. Vineetha, A. Aswathy, E. Shiju, K. Chandrasekharan and N. Manoj, *New J. Chem.*, 2020, **44**, 6142–6150.

63 S. Anandan, S. Manoharan, N. S. Narendran, T. S. Girisun and A. Asiri, *Opt. Mater.*, 2018, **85**, 18–25.